Six degrees of freedom coupled dynamic response of rotor with a transverse breathing crack

Bo Zhang & Yueming Li

Nonlinear Dynamics
An International Journal of Nonlinear Dynamics and Chaos in Engineering Systems

ISSN 0924-090X
Volume 78
Number 3

Nonlinear Dyn (2014) 78:1843-1861
DOI 10.1007/s11071-014-1563-2

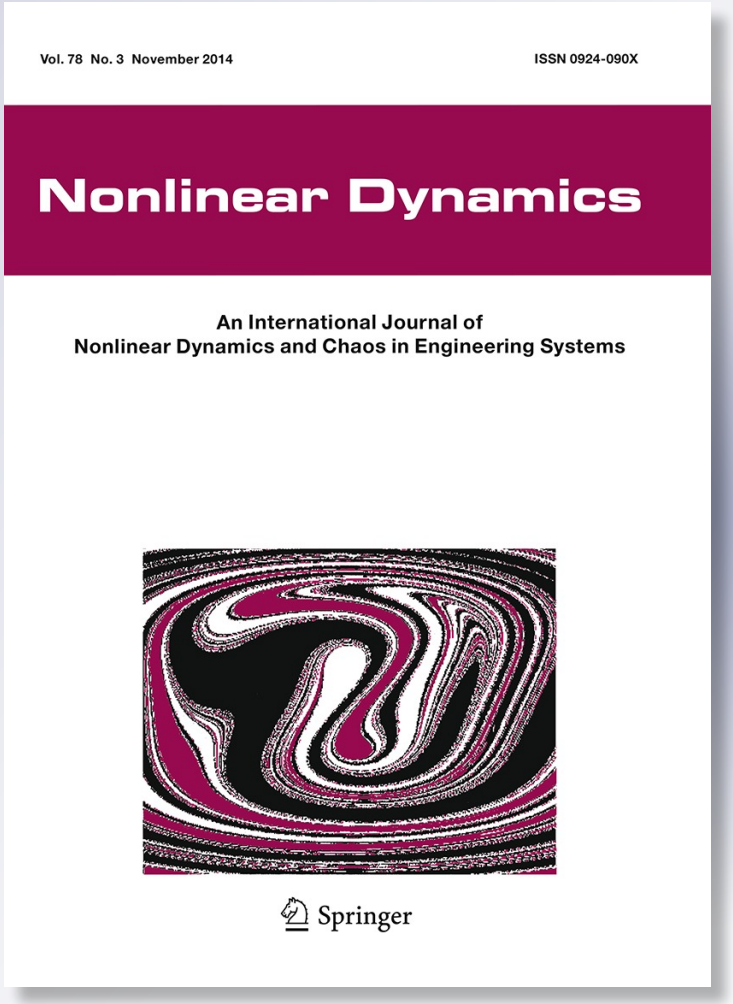

Springer

Nonlinear Dyn (2014) 78:1843–1861
DOI 10.1007/s11071-014-1563-2

ORIGINAL PAPER

Six degrees of freedom coupled dynamic response of rotor with a transverse breathing crack

Bo Zhang · Yueming Li

Received: 25 January 2014 / Accepted: 25 June 2014 / Published online: 16 July 2014

Abstract More coupling mechanisms between the six degrees of freedom (DOFs) are introduced by considering the contribution of the general transverse forces to stress intensity factor of mode I crack in predicting the crack additional flexibility matrix of the cracked rotor. And the obtained flexibility elements show a good agreement with the experiment result for a wide range of the crack depth ratio. Six DOFs coupled dynamic equations for cracked rotor are formulated by introducing three rotational DOFs. A response-dependent non-linear breathing crack model is applied to simulate the breathing behavior during operation in this paper. Numerical investigations are carried out to simulate the various parametric conditions on the dynamic characteristics of cracked rotor, including the crack depth, shaft slenderness ratio, and rotating speed ratio. A perturbation frequency component and its combinations with harmonic components are observed in the dynamic response obtained by six DOFs coupled models (SDCM). Some differences in evolution of whirling orbit obtained by SDCM and three DOFs coupled models are found, when the cracked rotor passes through the sub-critical speeds.

B. Zhang · Y. Li (✉)
State Key Laboratory for Strength and Vibration of Mechanical Structures, Xi'an Jiaotong University, Xi'an 710049, China
e-mail: liyueming@mail.xjtu.edu.cn

Keywords Cracked rotor · Local flexibility theorem · Coupled vibration · Breathing crack · Perturbation frequency components

1 Introduction

An increase in the power-to-weight ratio demand on rotor systems causes a severe stress field in the shaft. The fatigue crack of shaft is one of classic malfunctions in the rotor system, which can lead to a catastrophic failure if undetected at an early time. The dynamic behavior of a cracked rotor has drawn many researchers' attention since 1970s. The research works in this field have been well documented by Dimarogonas and Paipetis [1].

In most published research works, the crack in a rotor is considered as a reduction in stiffness. And the modification in stiffness due to the crack is often obtained based on strain energy release rate theory combined with linear fracture mechanics [2–6]. A systematic review of these techniques is presented by Papadopoulos [7]. Recently, some other techniques have been presented in modeling the cracked rotor in literature [8–13]. The dissimilar area moments of inertia in the crack section are used to obtain the variation of stiffness during rotation in [8–11]. Kulesza and Sawicki [12,13] introduce a new model of the cracked rotating shaft based on the rigid finite element method. In their model, the crack is presented as several dozen spring-damping elements of variable stiffness connecting two

sections of the shaft. This technique can be applied to simulate the propagation and breathing mechanism of the crack, effortlessly and intuitively.

During the rotation of the cracked rotor, the static deflection due to some complicated loads on the structure (such as self-weight, operational load, friction, and non-uniform thermal load) combined with the self-vibration effect may cause the crack to open and close gradually depending on the real-time response of the rotor. Some researchers [4,14] assumed that the crack remains open during the revolution. There also exist many research works applying a bilinear dynamic model to study the response of the cracked rotor. Qin et al. [15] used a two degrees of freedom (DOFs) piecewise linear system to model the cracked rotor, and observed a grazing bifurcation that exists in the response. Ballo [16] modeled the crack as a rotational spring element with bilinear stiffness properties depending on whether the curvature was positive or negative. Wauer [17] explored the dynamics of a cracked, distributed parameter rotor component. The geometric discontinuity due to the crack is replaced by a load discontinuity, and the open/close condition is formulated to simulate the breathing crack. Lee et al. [18] decided whether the crack is opened or closed by the sign of the displacement component in the weaker axis. Chondros et al. [19] assumed that the transition period from fully open to fully closed occurs at times when the structure returns to its undeformed shape. In addition, in some other research works, the crack is allowed to partially open or closed. For instance, Mayes and Davies [20] presented a harmonic variation function of angle position of the rotor to describe the reduction of stiffness in the weaker axis when the crack is partially open or closed. Chen and Dai [21] utilized an equivalent linear-spring model to describe the cracks, and represented the breathing of the crack with a series truncated time-varying cosine series. Al-Shudeifat and Butcher [9] proposed two new breathing functions to represent the actual breathing effect on the cracked element stiffness matrix. Jun et al. [3] proposed a two DOFs response-dependent breathing crack model. This model iteratively estimates the status of the crack closure using forces acting on the crack section. Darpe et al. [2,22] extended the breathing crack modeling of Jun et al. [3] to include the axial coordinate. In their work, the amount of crack open part is decided through calculating the stress intensity factor (SIF) at a series of given nodes along the crack edge. Darpe et al.'s later experimental work [23] proved the accuracy of this breathing crack model. So this non-linear crack breathing model is applied in the present work. However, in their work, only translational DOFs (two lateral translations and an axial translation) were considered, and the rotational DOFs (two bending angles and torsion angle of the crack section) were omitted. Dimarogonas and his colleagues [4,24] derived the 6×6 crack additional flexibility matrix of a cracked rotor based on the strain energy release rate method. A lot of researchers [25–31] investigated the parametric instability of a cracked rotor based on Dimarogonas' perfect work, while there are few studies on simulation of Jeffcott cracked rotor's six coupled DOFs dynamic response using a response-dependent non-linear breathing crack model reported in literature. Few investigators have tackled the problem about the effects of the coupling mechanics between rotational DOFs and translational DOFs on the dynamic behavior of cracked rotor. It is the purpose of this paper to supplement this gap in the literature.

In this paper, an attempt is made to calculate a more accurate crack local flexibility matrix with more coupled elements by considering the contribution of the transverse general forces to the SIF of mode I crack. This attempt is proved to be valid through the comparison between the numerical results [24] and Bush's experiment results [32]. The opening and closing of crack are governed by the sign of SIF at the crack edge, so the stiffness matrix is response dependent. Coupled equations of motion involving six DOFs are solved by numerical integration using Runge–Kutta method. The influences of slenderness (sld) ratio, crack depth, and rotating speed ratio on the dynamic behavior of crack are revealed. A series of perturbation frequency components are observed in the dynamic response.

2 Mathematic modeling of the cracked rotor

2.1 Model of Jeffcott cracked rotor

Consider a rigid disk of mass m mounted at mid-span of a massless elastic shaft in radially rigid bearings as shown in Fig. 1; it is assumed that a surface transverse crack locates at the mid-span of the shaft, and Fig. 2 shows the coordinate system used in the present paper. The coordinates x, y and ξ, η are the stationary and rotating ones, respectively. The coordinate u represents

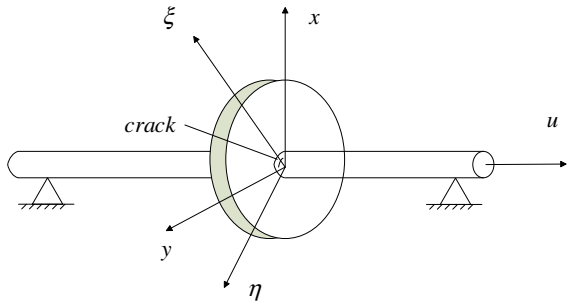

Fig. 1 Sketch of a Jeffcott cracked rotor

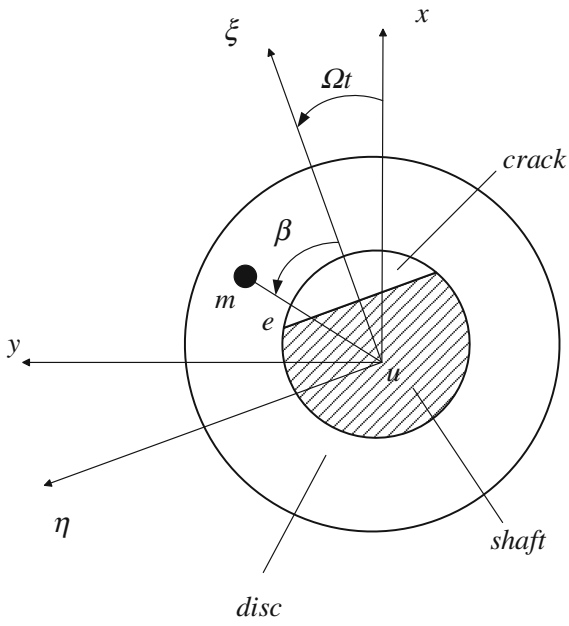

Fig. 2 The stationary and rotating coordinate systems

axial axis. e is the eccentricity of the center of the disk mass m from the geometric center of the disk. β is the orientation angle of the eccentricity from the ξ axis in the direction of shaft rotation, and Ω is the rotational speed.

2.2 Local flexibility of a cracked shaft

Consider that the cracked shaft is loaded with six general forces (shear forces Q_1, Q_2, axis force Q_3, bending moments Q_4, Q_5, and torsion moment Q_6) related to six DOFs (transverse translations ξ, η, axial translation u, bending rotation θ_ξ, θ_η, *and* torsional rotation θ_u) at the mid-span, respectively, as shown in Fig. 3.

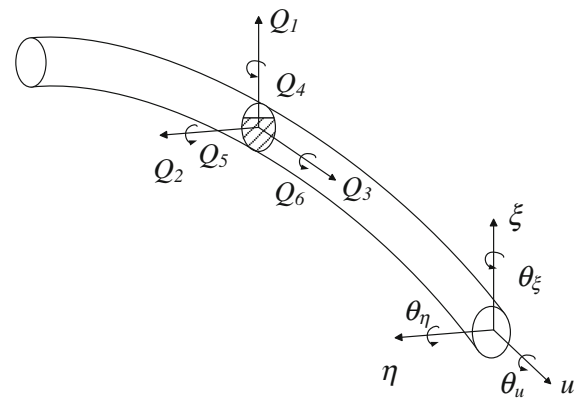

Fig. 3 Cracked shaft loaded with six general forces

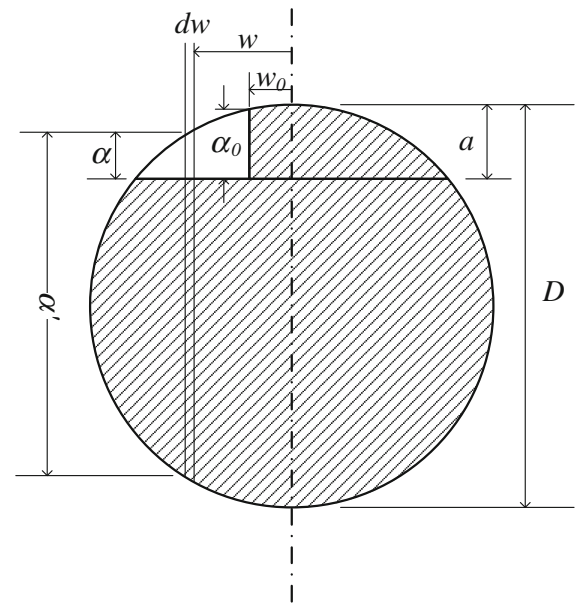

Fig. 4 Cracked section geometry

It is assumed that the shaft section consists of elementary strips with varying height, and there is no traction between strips. These strips are perpendicular to the crack tip and parallel to the axis of symmetry of the cylindrical shaft. Under six general forces, the stress along the tip of crack may have different values. Hence, the SIF is expressed as a function of coordinate w as shown in Fig. 4. The position of crack closure line (CCL) [33], an imaginary line that separates the closed part from the open part of the crack (i.e., the line $w = w_0$ in Fig. 4), varies continuously during the rotation. So the cracked additional flexibilities vary with the rotation. Initially, the crack is fully closed due to

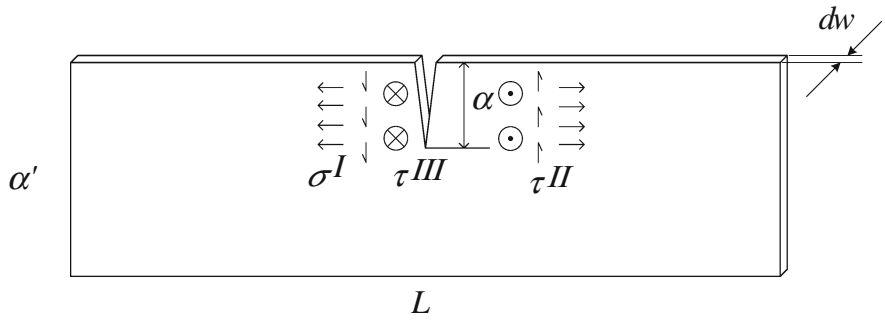

Fig. 5 Schematic drawing of elementary strip

self-weight, and 100 nodes are set along the crack tip in the present study. The position of CCL travels along the crack edge during the rotation. When the crack is opening from b to $-b$, statuses 1–100 are employed to describe the crack at unique moment. When the crack is closing from $-b$ to b, statuses 101–200 are used. For example, the half open and half closed condition (left half part open) is defined as status 50, and the status 150 indicates the half closed and half open condition (right half part open).

Apart from the symmetry of shaft w, a strip is taken out to study carefully. Assume that this strip is of length L, width dw, and height α', paralleling to the symmetry of the shaft, and there is an edge crack of depth α on it (as shown in Fig. 5). The stress fields (σ^{I}, τ^{II}, τ^{III}) effect the three modes of crack, respectively.

Under the general transverse forces Q_1 and Q_2, the strip tends to bend. Not only shear stress but also the normal stress appear on the crack section of the given strip. So the contribution of these two general forces on mode I crack is taken into account extra in the present study. With Q_1 acting on the shaft, the normal stress is linear distribution along the section of strip, while for Q_2, the normal stress is uniform. And the SIFs of mode I crack due to Q_1 and Q_2 could be written as the following equations according to the handbook [34]:

$$K_1^{\mathrm{I}} = \sigma_1^{\mathrm{I}}\sqrt{\pi\alpha}F_1(\alpha/\alpha'),$$
$$\sigma_1^{\mathrm{I}}(w) = \frac{Q_1 L}{4}\frac{\alpha'}{2}\Big/\left(\frac{\pi R^4}{4}\right), \tag{1}$$
$$K_2^{\mathrm{I}} = \sigma_2^{\mathrm{I}}\sqrt{\pi\alpha}F_2(\alpha/\alpha'),$$
$$\sigma_2^{\mathrm{I}}(w) = \frac{Q_2 L}{4}w\Big/\left(\frac{\pi R^4}{4}\right). \tag{2}$$

Other SIFs due to the general forces are calculated by the method presented in previous works [4,24]. For the purpose of completeness and consistent of symbol, SIFs of three modes of crack are coordinated in Appendix 1.

According to Castigliano's theorem, the strip crack additional displacement can be written as [34]

$$u_i^{\mathrm{strip}} = \frac{\partial}{\partial Q_i}\left[\int J(\alpha)\mathrm{d}A\right], \tag{3}$$

in which J stands for strain energy release rate:

$$J = \frac{1}{E'}\left[\left(\sum_{i=1}^{6} K_i^{\mathrm{I}}\right)^2 + \left(\sum_{i=1}^{6} K_i^{\mathrm{II}}\right)^2\right] + \frac{(1+\nu)}{E}\left(\sum_{i=1}^{6} K_i^{\mathrm{III}}\right)^2, \tag{4}$$

where $E' = E/(1-\nu)$ for plane strain, E is the modulus of elasticity, and ν is the Poisson ratio.

The local flexibility of strip due to the crack is, by definition,

$$g_{ij}^{\mathrm{strip}} = \frac{\partial u_i^{\mathrm{strip}}}{\partial Q_j} = \frac{\partial^2}{\partial Q_i \partial Q_j}\left[\int_0^{\alpha} J(\alpha)\mathrm{d}\alpha\right]. \tag{5}$$

By integrating (5) along the crack width $2b$, we get the crack additional flexibility of rotor

$$g_{ij}^{\mathrm{crack}} = \frac{\partial u_i^{\mathrm{crack}}}{\partial Q_j} = \frac{\partial^2}{\partial Q_i \partial Q_j}\left[\int_{-b}^{b}\int_0^{\alpha} J(\alpha)\mathrm{d}A\right]. \tag{6}$$

Combining the expression of SIFs with the Eqs. (4) and (6), it yields elements of the 6×6 crack additional flexibility matrix (shown in Appendix 1). Note that the area integrations are only conducted at the open part of crack.

In the present study, the contribution of the transverse forces to the SIFs of mode I crack, i.e., Eqs. (1) and (2), is taken into account, resulting in more non-zero elements in the flexibility matrix (such as

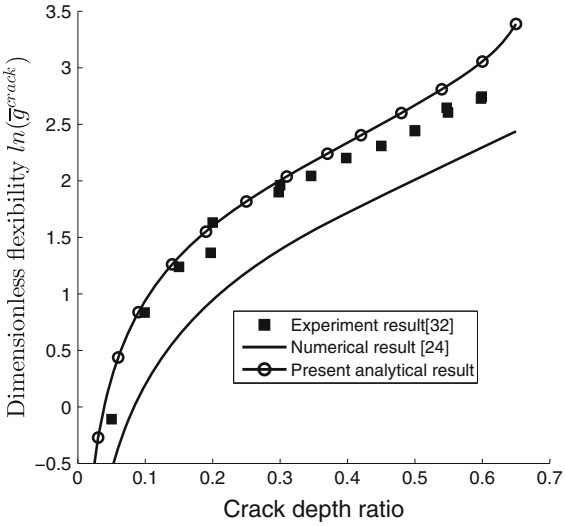

Fig. 6 Comparison of the present analytical result with previous result

g_{12}^{crack}, g_{13}^{crack}, g_{14}^{crack}, g_{15}^{crack}, g_{23}^{crack}, g_{24}^{crack}, and their symmetrical ones). For fully open cracked rotor, the flexibility matrix elements are only depended on the crack depth ratio $\bar{a} = a/D$. The dimensionless crack additional flexibility elements are defined as follows:

$$\begin{aligned}
\bar{g}_{kl}^{\text{crack}} &= \frac{\pi E R g_{kl}^{\text{crack}}}{1-\upsilon^2}(k = 1,\ 2,\ 3;\ l = 1,\ 2,\ 3),\\
\bar{g}_{kl}^{\text{crack}} &= \bar{g}_{lk}^{\text{crack}} = \frac{\pi E R^2 g_{kl}^{\text{crack}}}{1-\upsilon^2}\\
&\quad (k = 1,\ 2,\ 3;\ l = 4,\ 5,\ 6),\\
\bar{g}_{kl}^{\text{crack}} &= \frac{\pi E R^3 g_{kl}^{\text{crack}}}{1-\upsilon^2}(k = 4,\ 5,\ 6;\ l = 4,\ 5,\ 6).
\end{aligned} \tag{7}$$

The variation of the first diagonal flexibility matrix element, $\bar{g}_{11}^{\text{crack}}$, with depth ratio is plotted in Fig. 6 for comparison between the present work and previous studies. It is obvious that the curve obtained in the present study is a little higher than that obtained by Papaeconomou and Dimarogonas [24], and is better accurate with Bush's experimental result [32] for a wide range of the crack depth ratio. This is due to the assumption that the transverse force Q_1 contributes to not only the mode II crack but also the mode I crack. The flexibility element $\bar{g}_{11}^{\text{crack}}$ consists of two parts corresponding to mode I crack and mode II crack, respectively. Further, if the general forces Q_i and Q_j can contribute the same mode of crack, then $\bar{g}_{ij}^{\text{crack}}$ is non-zero. For instance, Q_1, Q_2, Q_3, Q_4, and Q_5 make sense in forming mode I crack, so the corresponding DOFs, i.e., ξ, η, u, θ_ξ and θ_η, are coupled with each other.

Then, the variation of non-zero elements in dimensionless crack additional flexibility matrix with the moving of CCL position is illustrated in Fig. 7 for a specific depth ratio ($\bar{a} = 0.4$). It is easy to find that when the crack is opened completely, namely the status 100, all of the diagonal elements reach to their peak value but several non-diagonal elements (such as $\bar{g}_{12}^{\text{crack}}$, $\bar{g}_{23}^{\text{crack}}$, $\bar{g}_{16}^{\text{crack}}$, $\bar{g}_{25}^{\text{crack}}$, $\bar{g}_{14}^{\text{crack}}$, $\bar{g}_{45}^{\text{crack}}$, and $\bar{g}_{34}^{\text{crack}}$) vanish. These non-diagonal elements reach to their peak value at the time when the crack is half opened. This is mainly due to that the crack section is symmetric about the axis ξ when fully opened, and the asymmetry level gets their largest value when the crack half opened. These variation characteristics are consistent with the crack finite element in [33]. These comparisons prove that it is necessary to consider the contribution of general transverse forces to mode I crack.

Above all, the additional flexibilities introduced by the crack have been calculated. While the flexibilities of uncracked shaft can be easily obtained based on the strength of materials:

$$\begin{aligned}
g_{11}^0 &= g_{22}^0 = \tfrac{L^3}{48EI_{\text{d}}},\\
g_{33}^0 &= \tfrac{L}{AE},\\
g_{44}^0 &= g_{55}^0 = \tfrac{L}{12EI_{\text{d}}},\\
g_{66}^0 &= \tfrac{L\kappa}{2GI_{\text{p}}},
\end{aligned} \tag{8}$$

where $A = \pi R^2$ is the area of the shaft section, $I_{\text{d}} = \pi R^4/4$ is the area moment of inertia, $I_{\text{p}} = \pi R^4/2$ is the polar moment of inertia, and $G = E/2(1+\nu)$ is the shear modulus. So the total flexibility coefficients matrix is obtained as follows:

$$\mathbf{G} = \mathbf{G}^{\text{crack}} + \mathbf{G}^0. \tag{9}$$

By inversing the flexibility coefficients matrix, the stiffness matrix can be written as

$$\mathbf{K} = \mathbf{G}^{-1}. \tag{10}$$

2.3 Six DOFs coupled equations of motion

Consider the Jeffcott rotor loaded with unbalance mass and its weight shown in Fig. 1. The stiffness matrix is obtained in rotating coordinate in previous section. The following transformation matrix is used to transform the equations of motion from the stationary coordinate to the rotating one.

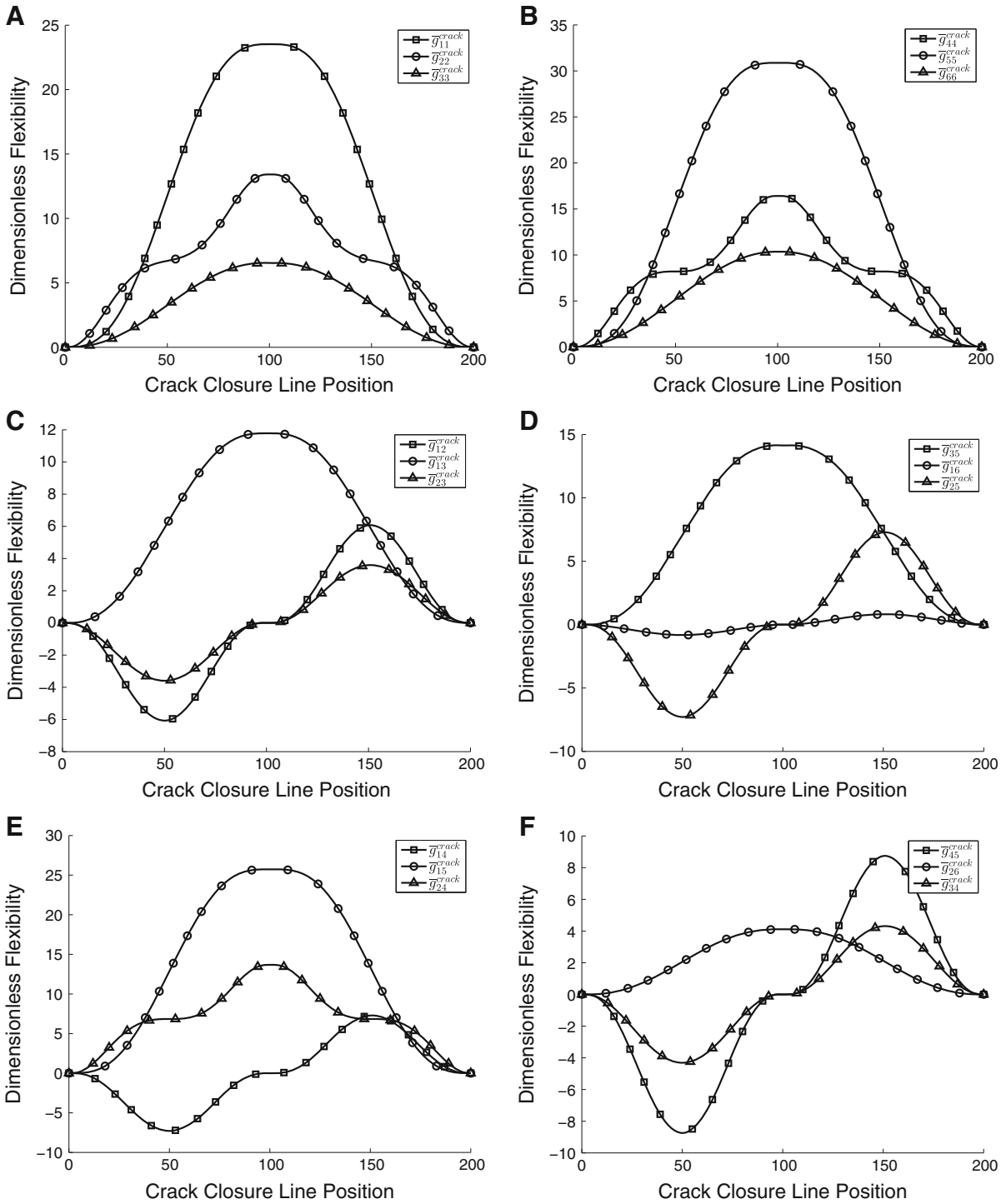

Fig. 7 Then, the variation of dimensionless crack additional flexibility matrix non-zero element with the moving of CCL ($\bar{a} = 0.4$)

$$\begin{Bmatrix} x \\ y \\ z \\ \theta_x \\ \theta_y \\ \theta_z \end{Bmatrix} = \begin{bmatrix} \cos(\Omega t) & \sin(\Omega t) & 0 & 0 & 0 & 0 \\ -\sin(\Omega t) & \cos(\Omega t) & 0 & 0 & 0 & 0 \\ 0 & 0 & 1 & 0 & 0 & 0 \\ 0 & 0 & 0 & \cos(\Omega t) & \sin(\Omega t) & 0 \\ 0 & 0 & 0 & -\sin(\Omega t) & \cos(\Omega t) & 0 \\ 0 & 0 & 0 & 0 & 0 & 1 \end{bmatrix} \begin{Bmatrix} \xi \\ \eta \\ u \\ \theta_\xi \\ \theta_\eta \\ \theta_u \end{Bmatrix}. \tag{11}$$

Then, the six DOFs coupled equations of motion can be expressed in the rotating coordinates as

$$\begin{aligned}
&m\left(\ddot{\xi} - 2\Omega\dot{\eta} - \Omega^2\xi\right) + c(\dot{\xi} - \Omega\eta) + k_{11}\xi + k_{12}\eta \\
&\quad + k_{13}u + k_{14}\theta_\xi + k_{15}\theta_\eta + k_{16}\theta_u \\
&\quad = m\varepsilon\Omega^2\cos\beta - mg\cos\Omega t, \\
&m\left(\ddot{\eta} + 2\Omega\dot{\xi} - \Omega^2\eta\right) + c(\dot{\eta} + \Omega\xi) + k_{21}\xi + k_{22}\eta \\
&\quad + k_{23}u + k_{24}\theta_\xi + k_{25}\theta_\eta + k_{26}\theta_u \\
&\quad = m\varepsilon\Omega^2\sin\beta + mg\sin\Omega t, \\
&m\ddot{u} + c_u\dot{u} + k_{31}\xi + k_{32}\eta + k_{33}u + k_{34}\theta_\xi + k_{35}\theta_\eta \\
&\quad + k_{36}\theta_u = 0, \\
&J_\mathrm{d}\left(\ddot{\theta}_\xi - 2\Omega\dot{\theta}_\eta - \Omega^2\theta_\xi\right) + c_\mathrm{d}\left(\dot{\theta}_\xi - \Omega\theta_\eta\right) + k_{41}\xi \\
&\quad + k_{42}\eta + k_{43}u + k_{44}\theta_\xi + k_{45}\theta_\eta + k_{46}\theta_u = 0, \\
&J_\mathrm{d}\left(\ddot{\theta}_\eta + 2\Omega\dot{\theta}_\xi - \Omega^2\theta_\eta\right) + c_\mathrm{d}\left(\dot{\theta}_\eta + \Omega\theta_\xi\right) + k_{51}\xi \\
&\quad + k_{52}\eta + k_{53}u + k_{54}\theta_\xi + k_{55}\theta_\eta + k_{56}\theta_u = 0, \\
&J_\mathrm{p}\ddot{\theta}_u + c_\mathrm{p}\dot{\theta}_u + k_{61}\xi + k_{62}\eta + k_{63}u + k_{64}\theta_\xi + k_{65}\theta_\eta \\
&\quad + k_{66}\theta_u = 0,
\end{aligned} \tag{12}$$

in which m is the mass of the disk; J_d and J_p are the area moment of inertia and the polar moment of inertia of the disk, respectively; and c, c_u, c_d, and c_p are the damping coefficients of lateral, axial, bending, and torsional vibrations, respectively. The stiffness elements k_{ij} are response dependent, resulting in the non-linear differential equations. In order to simplify the equations, following non-dimensional parameters are introduced.

$$\begin{aligned}
&\tau = \Omega t, \quad \zeta = \frac{c}{2m\omega_{11}}, \quad \zeta_u = \frac{c_u}{2m\omega_{33}}, \\
&\zeta_\mathrm{d} = \frac{c_\mathrm{d}}{2J_\mathrm{d}\omega_{44}}, \quad \zeta_\mathrm{p} = \frac{c_\mathrm{p}}{2J_\mathrm{p}\omega_{66}}, \\
&P_{ij} = \omega_{ij}/\Omega (i = 1, \ldots, 6, \ j = 1, \ldots, 6), \\
&P_i^0 = \omega_i^0/\Omega (i = 1, \ldots, 6),
\end{aligned} \tag{13}$$

where

$$\omega_i^0 = \begin{cases} \sqrt{k_i^0/m} & (i = 1, \ldots, 3), \\ \sqrt{k_i^0/J_\mathrm{d}} & (i = 4,\ 5), \\ \sqrt{k_i^0/J_\mathrm{p}} & (i = 6), \end{cases} \tag{14}$$

$$\omega_{ij} = \begin{cases} \sqrt{k_{ij}/m} & (i = 1, \ldots, 3), \\ \sqrt{k_{ij}/J_\mathrm{d}} & (i = 4,\ 5), \quad j = 1, \ldots, 6, \\ \sqrt{k_{ij}/J_\mathrm{p}} & (i = 6) \end{cases}$$

k_i^0 is the ith diagonal element in the stiffness matrix of uncracked shaft, and k_{ij} is the element in the response-dependent stiffness matrix of crack shaft. In the present study, the rotating speed ratio of the rotor is defined as the ratio of the rotating speed to the first bending critical frequency, i.e., $1/P_1^0$. The simplified equations of motion are obtained through a series of mathematical manipulations:

$$\begin{aligned}
&\frac{\mathrm{d}^2\xi}{\mathrm{d}\tau^2} + 2\zeta P_1^0\frac{\mathrm{d}\xi}{\mathrm{d}\tau} - 2\frac{\mathrm{d}\eta}{\mathrm{d}\tau} + \left(P_{11}^2 - 1\right)\xi \\
&\quad - \left(2\zeta P_1^0 - P_{12}^2\right)\eta + P_{13}^2 u + P_{14}^2\theta_\xi + P_{15}^2\theta_\eta \\
&\quad + P_{16}^2\theta_u = e\cos\beta - g/\Omega^2\cos\tau, \\
&\frac{\mathrm{d}^2\eta}{\mathrm{d}\tau^2} + 2\zeta P_2^0\frac{\mathrm{d}\eta}{\mathrm{d}\tau} + 2\frac{\mathrm{d}\xi}{\mathrm{d}\tau} + \left(2\zeta P_1^0 + P_{21}^2\right)\xi \\
&\quad - \left(P_{22}^2 - 1\right)\eta + P_{23}^2 u + P_{24}^2\theta_\xi + P_{25}^2\theta_\eta + P_{26}^2\theta_u \\
&= e\sin\beta + g/\Omega^2\sin\tau, \\
&\frac{\mathrm{d}^2 u}{\mathrm{d}\tau^2} + 2\zeta_u P_3^0\frac{\mathrm{d}u}{\mathrm{d}\tau} + P_{31}^2\xi + P_{32}^2\eta + P_{33}^2 u + P_{34}^2\theta_\xi \\
&\quad + P_{35}^2\theta_\eta + P_{36}^2\theta_u = 0, \\
&\frac{\mathrm{d}^2\theta_\xi}{\mathrm{d}\tau^2} + 2\zeta_\mathrm{d} P_4^0\frac{\mathrm{d}\theta_\xi}{\mathrm{d}\tau} - 2\frac{\mathrm{d}\theta_\eta}{\mathrm{d}\tau} + P_{41}^2\xi + P_{42}^2\eta + P_{43}^2 u \\
&\quad + \left(P_{44}^2 - 1\right)\theta_\xi - \left(2\zeta_\mathrm{d} P_4^0 - P_{45}^2\right)\theta_\eta + P_{46}^2\theta_u = 0, \\
&\frac{\mathrm{d}^2\theta_\eta}{\mathrm{d}\tau^2} + 2\zeta_\mathrm{d} P_5^0\frac{\mathrm{d}\theta_\eta}{\mathrm{d}\tau} + 2\frac{\mathrm{d}\theta_\xi}{\mathrm{d}\tau} + P_{51}^2\xi + P_{52}^2\eta \\
&\quad + P_{53}^2 u + \left(2\zeta_\mathrm{d} P_5^0 + P_{54}^2\right)\theta_\xi - \left(P_{55}^2 - 1\right)\theta_\eta \\
&\quad + P_{56}^2\theta_u = 0,
\end{aligned} \tag{15}$$

$$\frac{\mathrm{d}^2\theta_u}{\mathrm{d}\tau^2} + 2\zeta_\mathrm{p} P_6^0 \frac{\mathrm{d}\theta_u}{\mathrm{d}\tau} + P_{61}^2\xi + P_{62}^2\eta + P_{63}^2 u + P_{64}^2\theta_\xi + P_{65}^2\theta_\eta + P_{66}^2\theta_u = 0.$$

3 Breathing behavior of crack

The crack breathing behavior may occur due to the combined effect of static load and vibration amplitude, while the cracked shaft rotates. There exists a series of partial opening and closing statuses between the completely open and completely closed states of the crack. The solution process for solving the motion equations (15), which also govern the status of the crack, is presented in this section.

Assume that the initial displacement is the static deflection of the rotor under self-weight, and the crack is completely closed at the beginning. So the initial stiffness is equal to that of an uncracked shaft. Then, the general force vector can be evaluated in the rotating coordinate:

$$\mathbf{Q} = \mathbf{K}\left[\xi,\ \eta,\ u,\ \theta_\xi,\ \theta_\eta,\ \theta_u\right]_{\mathrm{init}}^{\mathrm{T}}. \tag{16}$$

100 nodes are set along the tip of the crack. Each of these nodes is the potentially possible position of the CCL. The SIFs at these 100 nodes are evaluated from the Eqs. (1), (2), and Appendix 1. Then, the total SIF of mode I crack is obtained easily.

$$K^{\mathrm{I}} = \sum_{n=1}^{6} K_n^{\mathrm{I}}. \tag{17}$$

Positive total SIF indicates that the crack opens at this node, while the negative indicates that the crack closes at this node. The position where the total SIF changes its sign is just the CCL position. All strips where the SIF is positive make up the open part of the crack, i.e., the integral domain of the additional flexibility. By inversing the flexibility matrix, the stiffness matrix is obtained. Then, the equations of motion Eq. (15) are numerical integrated using variable-step Runge–Kutta method for a given short time span (one degree of rotation in the present study) during which the stiffness is assumed to be constant. In order to get more accurate response, the relative error tolerance is set to a very low level, i.e., 1.0e−10 in the present study. Only the displacements and velocities at the end of each time span are stored and used as initial conditions for next time span. Using the transformation matrix, the status can be transformed into the stationary coordinate, and then the new general force vector is calculated. These forces are used to evaluate SIFs at the given nodes, and eventually, the next set of stiffness values is obtained, which are used in the equations of motion for the new time span. In another word, response is used to evaluate stiffness which governs the next set of response in turn. Repeat this series of calculations until time axis reach at the terminal point.

4 Numerical results

In this section, several numerical investigations are carried out to study the dynamic characteristics of cracked rotor. All the parameters used are given in Table 1.

First, unbalance response of an uncracked rotor with rotating speed ratio of $1/P_1^0 = 0.3$ is investigated. The first critical frequency of the given rotor can be calculated to be 390.55 Hz, so the rotation speed of the rotor is 117.16 Hz. Figure 8 illustrates that only the rotation speed component, namely 1X, is contained in the vertical and horizontal vibration. Figure 8a1, b1 shows the time domain response, and Fig. 8a2, b2 shows the corresponding frequency spectra in vertical and horizontal, respectively. The response of other DOFs is zero, due to symmetry in physics for an uncracked rotor, so no coupling mechanism between lateral DOFs (x, y) and other DOFs is introduced.

For comparison, the unbalance response of a cracked rotor running at the same speed is studied. The crack depth ratio of the rotor is $\bar{a} = 0.3$. In this case, all six DOFs are coupled, and the stiffness coefficients in

Table 1 Details of the rotor parameters

Description	Values
Radius of the shaft	7.5e−3 m
Radius of the disk	2.0e−2 m
Length of the shaft	0.16 m
Mass of the disk	1.0 kg
Eccentricity of the mass unbalance	2.0e−3 m
Phase unbalance	0 rad
Young's modulus of elasticity	2.0677e11 N/m^2
Poisson ratio	0.3
Coefficient of damping (ζ, ζ_u, ζ_d, ζ_p)	0.05
Acceleration of gravity	9.8 m/s^2

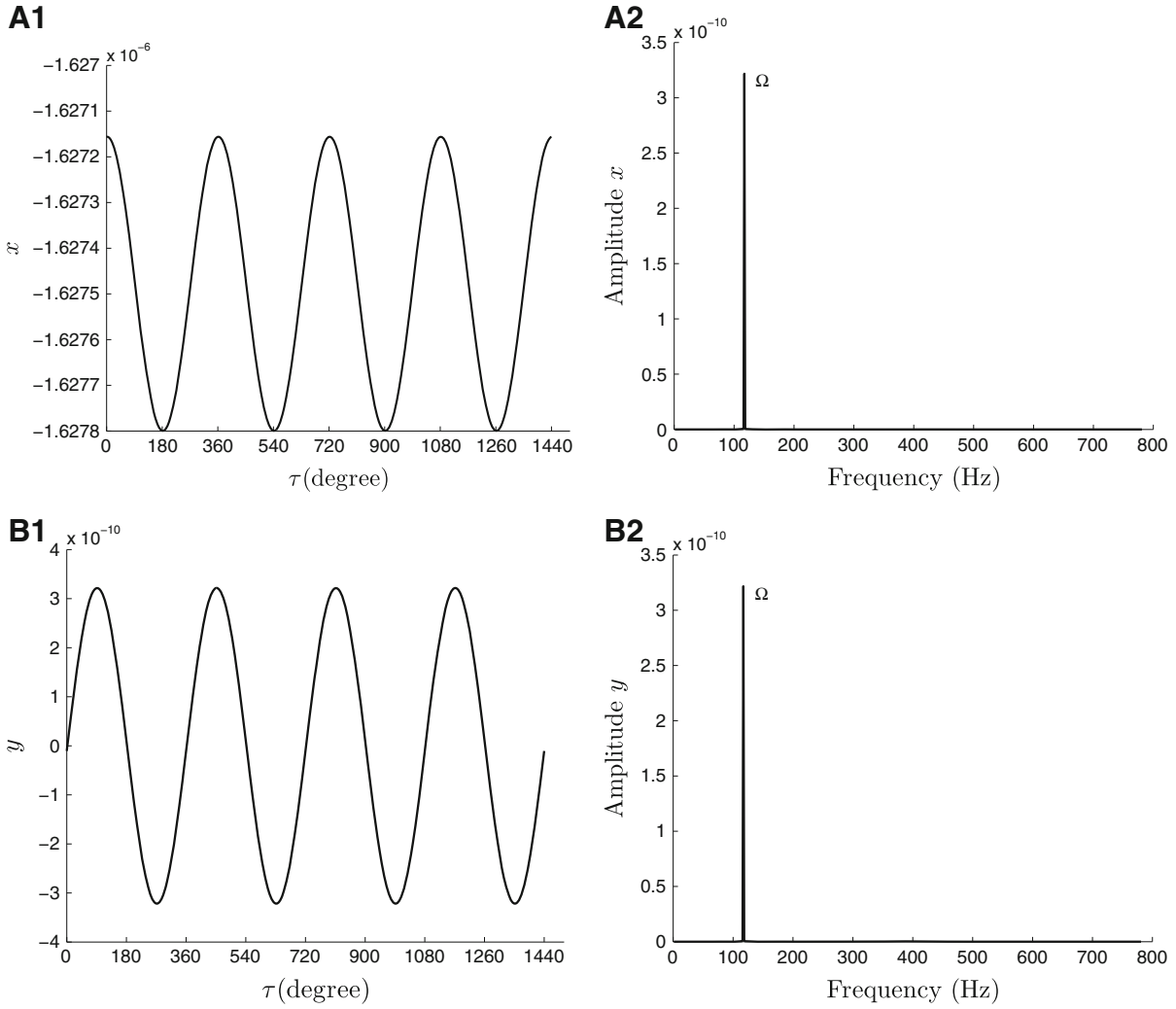

Fig. 8 Unbalance response of an uncracked rotor with rotating speed ratio of $1/P_1^0 = 0.3$. **a1** Time domain response in x. **b1** Time domain response in y. **a2** Frequency domain response in x. **b2** Frequency domain response in y

Eq. (15) are varying all the time during the rotation. The response of all six DOFs in time domain and frequency domain is shown in Fig. 9. The first three harmonic components are observed in the frequency spectra of all six DOFs, and 1X is very strong and dominating. This is well known in previous studies. In addition, some other new frequency components could also be observed on both sides of every harmonic component. In the present study, perturbation frequency ω_b is defined to describe these frequency components. To avoid confusion in identification, ω_b is limited which must be less than half of the rotation speed. In this case, ω_b is obtained to be 39.1 Hz from the frequency spectra. And it is easy to found that these newly found frequency components are just the combination between the perturbation frequency and harmonic frequencies. These frequency components are not reported in the literature before.

The same case is also simulated by three DOFs coupled models (TDCM), namely neglecting the coupling mechanism by three rotational DOFs. The dynamic response in frequency domain is displayed in Fig. 10. The frequency spectra are only contained several harmonic components. By comparing the frequency spectra obtained by six DOFs coupled models (SDCM; Fig. 9a2, b2) and TDCM (Fig. 10a, b), it could be con-

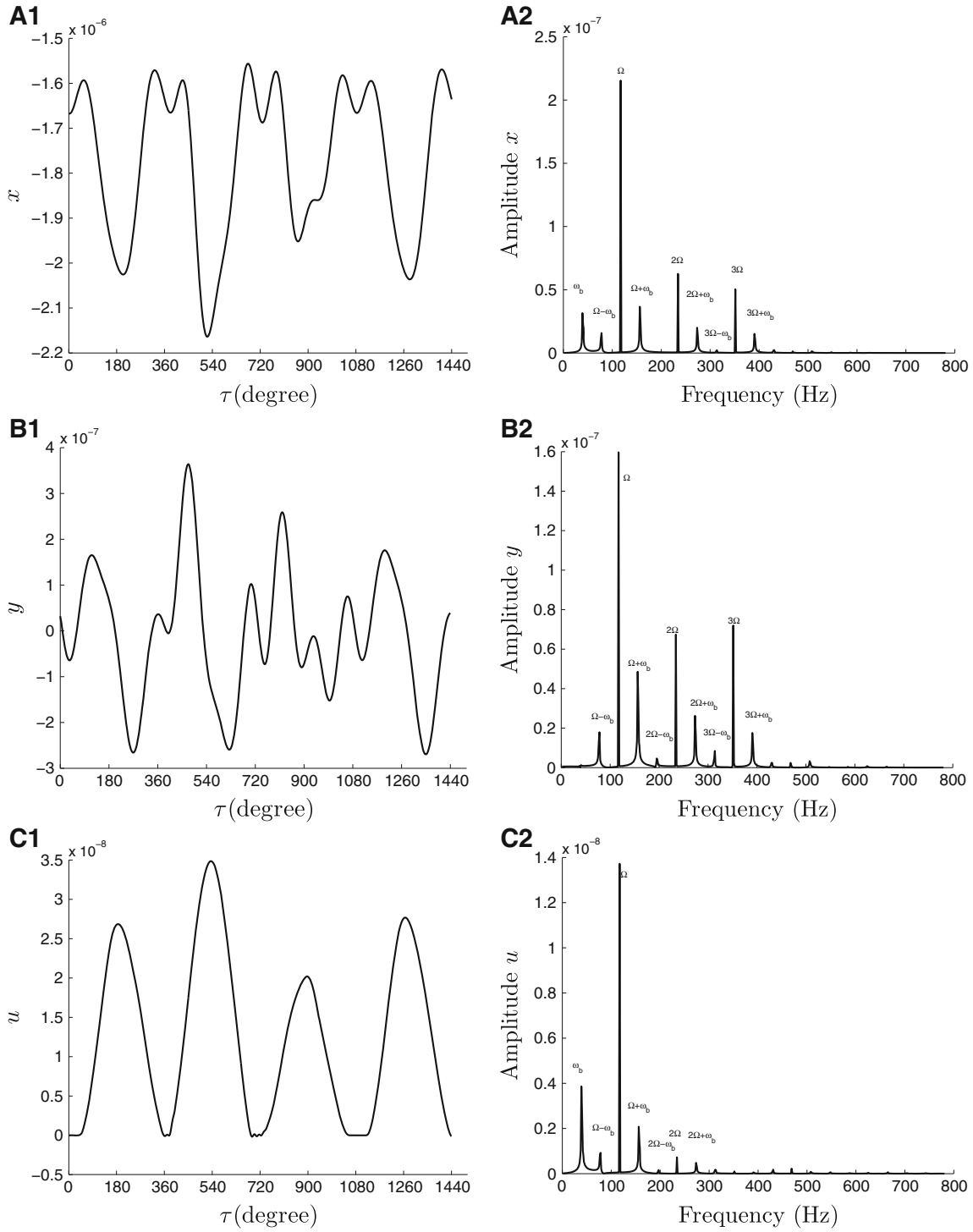

Fig. 9 Unbalance response of an cracked rotor (depth ratio of $\bar{a} = 0.3$) with rotating speed ratio of $1/P_1^0 = 0.3$ applied with SDCM. **a1** Time domain response in x. **b1** Time domain response in y. **c1** Time domain response in u. **d1** Time domain response in θ_x. **e1** Time domain response in θ_y. **f1** Time domain response in θ_u. **a2** Frequency domain response in x. **b2** Frequency domain response in y. **c2** Frequency domain response in u. **d2** Frequency domain response in θ_x. **e2** Frequency domain response in θ_y. **f2** Frequency domain response in θ_u

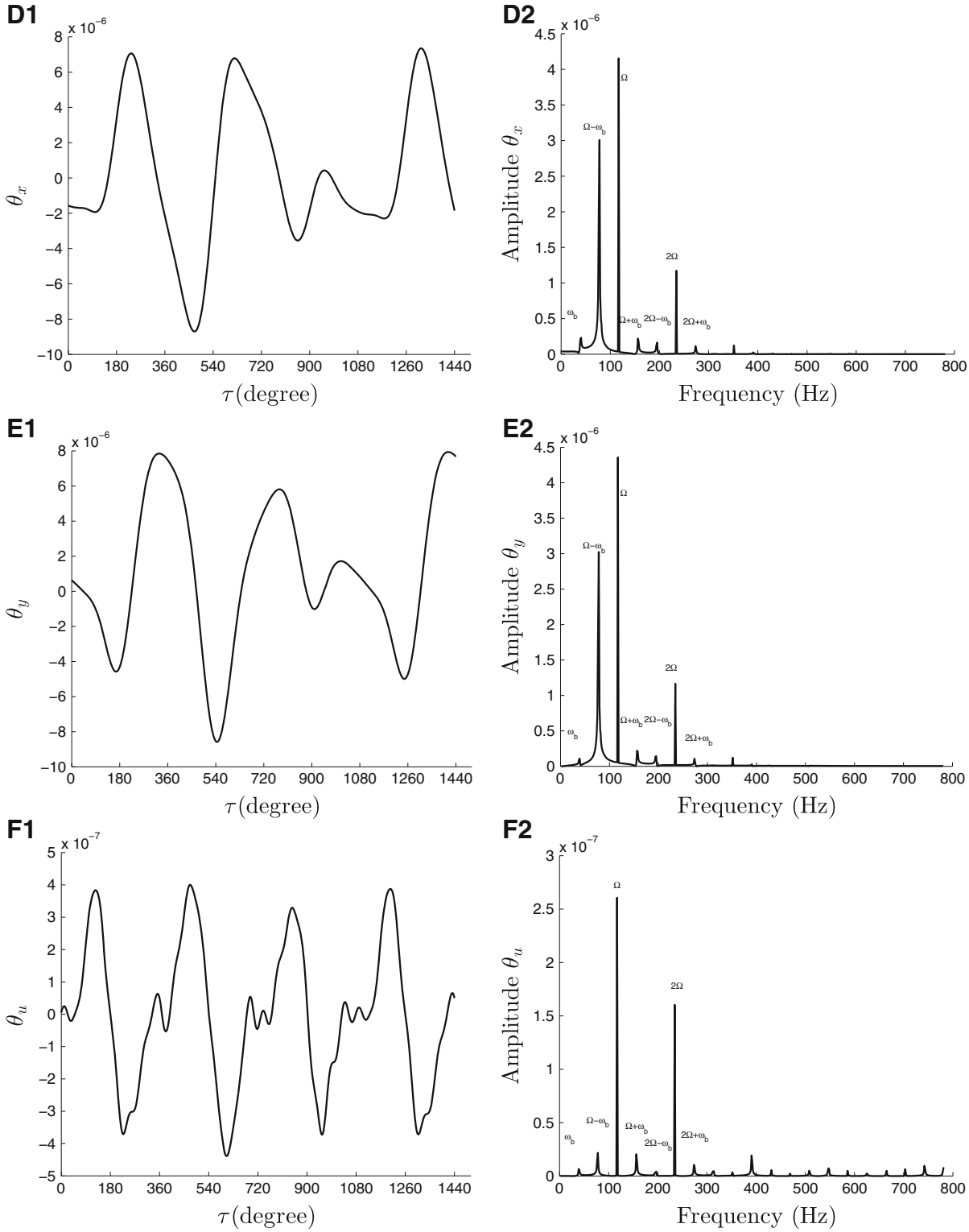

Fig. 9 continued

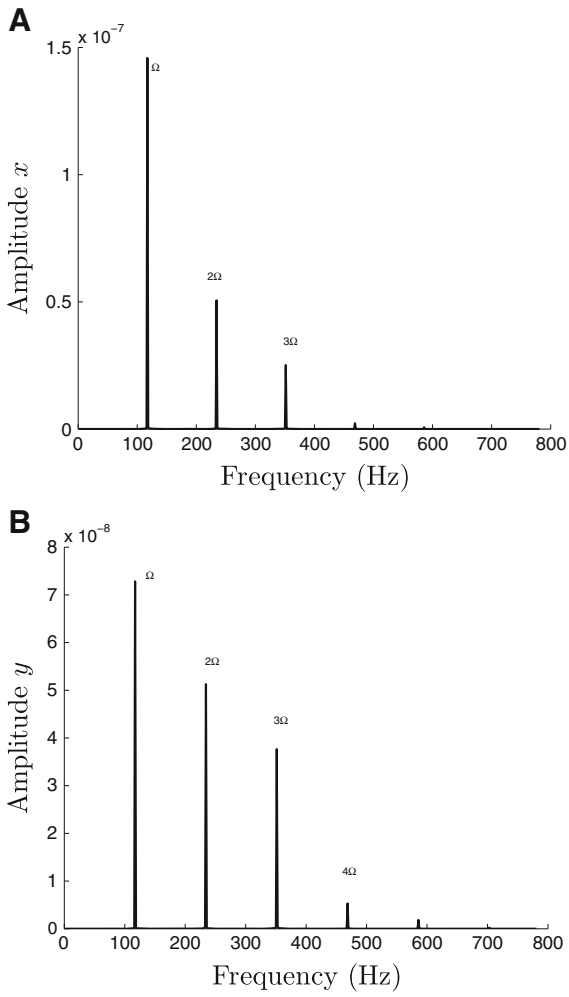

Fig. 10 Unbalance response of an cracked rotor (depth ratio of$\bar{a} = 0.3$) with rotating speed ratio of $1/P_1^0 = 0.3$ applied with TDCM. **a** Frequency domain response in x. **b** Frequency domain response in y

cluded that the perturbation frequency components are introduced by coupling mechanism between rotational DOFs and translational DOFs.

To find the relationship between perturbation frequency ω_b and system parameters, the dynamic response is calculated on the various parametric conditions. Figure 11 discovers the variation of perturbation frequency with rotating speed ratio for the cracked rotor with different sld ratios. In the present study, the dimensionless sld is defined as the ratio between the length and diameter of the rotor for convenience, namely $r_{\text{sld}} = L/D$. It is easy to find that the perturbation frequency increases rapidly with rotating speed

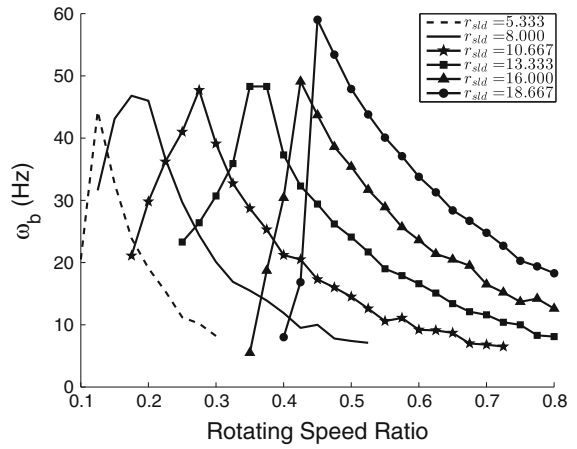

Fig. 11 The variation of the perturbation frequency with rotating speed ratio for different slenderness

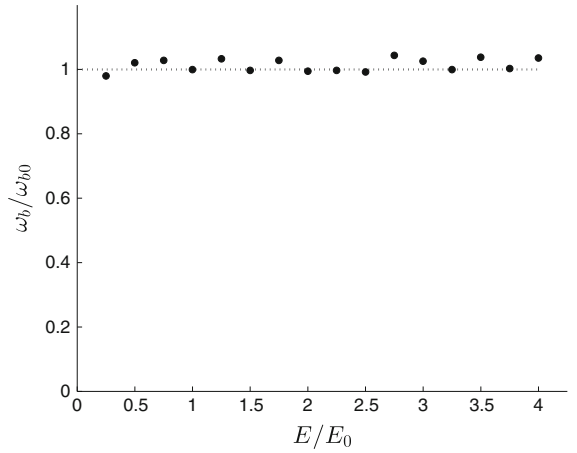

Fig. 12 The variation of the perturbation frequency with Young's Modulus

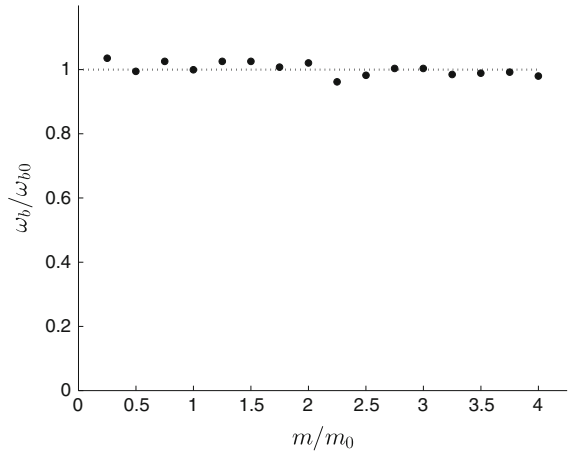

Fig. 13 The variation of the perturbation frequency with the mass of the disk

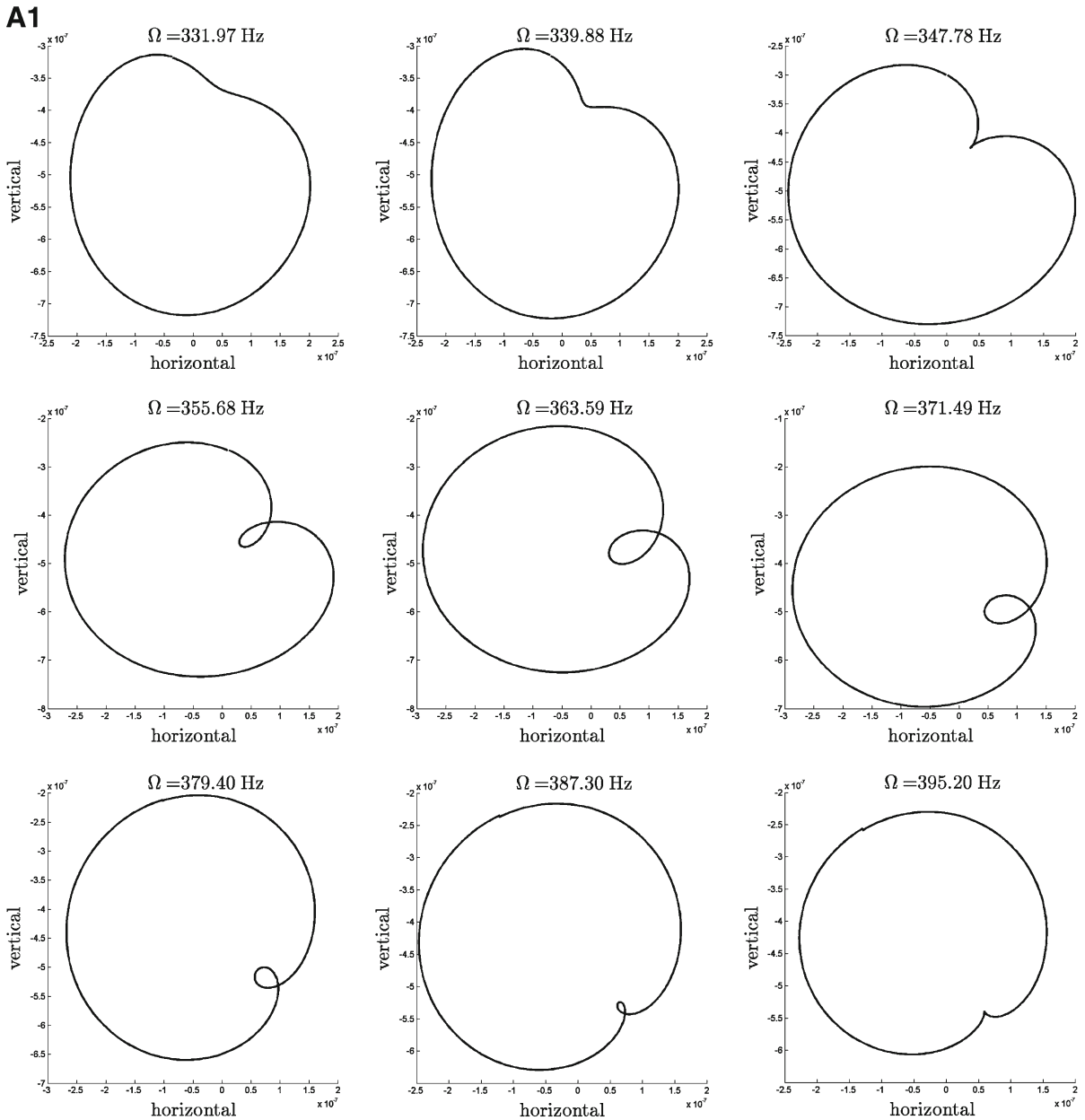

Fig. 14 Evolution of the orbit during the passage through 1/3 and 1/2 of the first critical rotating speed by SDCM (**a1**, **b1**) and TDCM (**a2**, **b2**). **a1** Evolution of the orbit during the passage through 1/2 of the first critical rotating speed obtained by TDCM. **b1** Evolution of the orbit during the passage through 1/3 of the first critical rotating speed obtained by TDCM. **a2** Evolution of the orbit during the passage through 1/2 of the first critical rotating speed obtained by SDCM. **b2** Evolution of the orbit during the passage through 1/3 of the first critical rotating speed obtained by SDCM

in low-speed range and then decreases slowly in high-speed range. When the rotating speed is high enough, these perturbation frequency components join to the harmonic components nearby. For the slender cracked rotors, the process of this evolution seems to flow to high-speed direction. Controlling variables method is applied to study the influence of other parameters on this perturbation frequency. We choose a general case

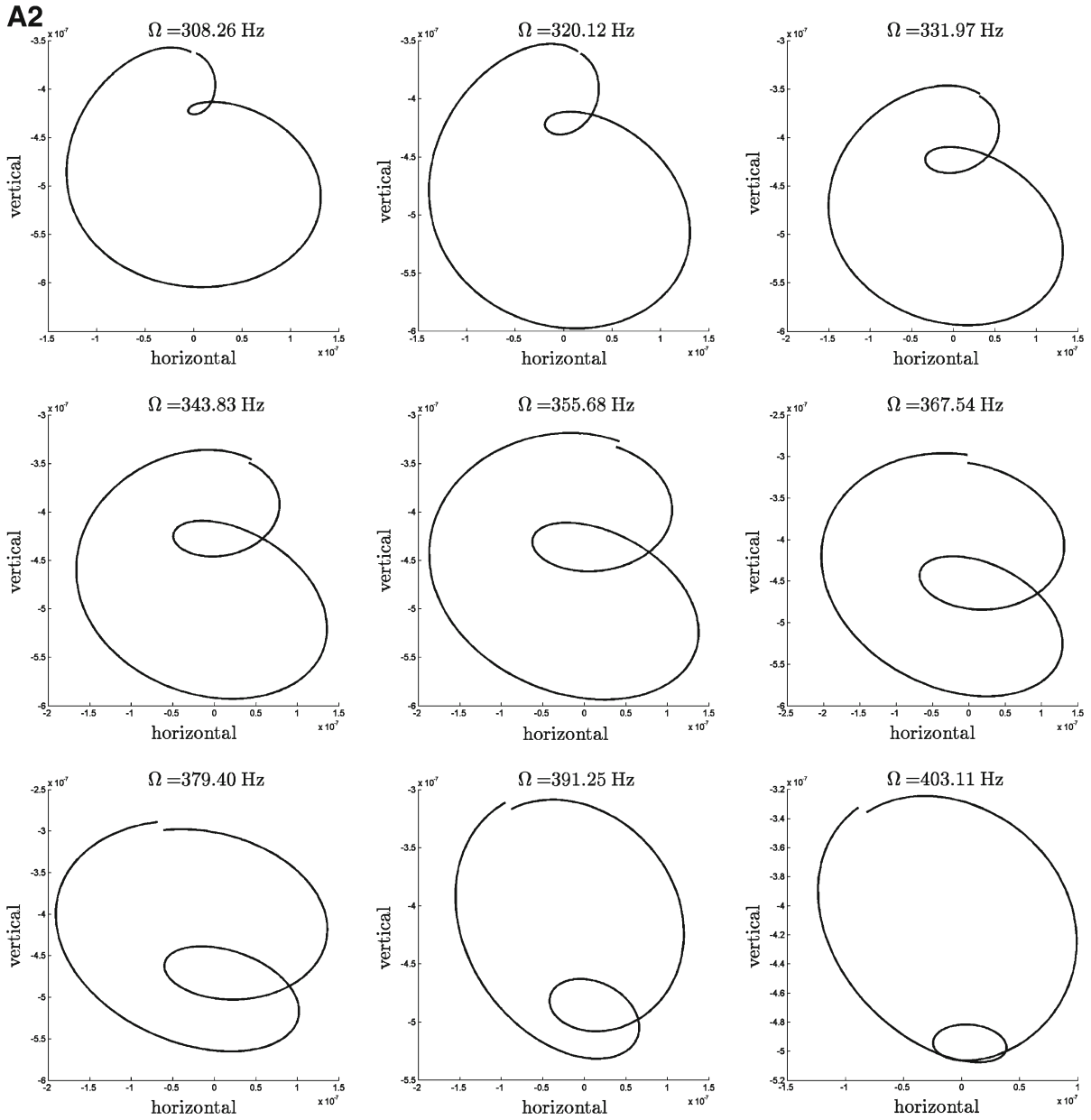

Fig. 14 continued

(given in Table 1) as the contrast, and vary the Young's modulus and the mass of the disk in a wide range, respectively. Figures 12 and 13 discover that the perturbation frequency is independent of Young's modulus of the rotor and the mass of the disk.

The numerical investigations conducted above could be summarized as follows. When coupling mechanism between lateral displacement DOFs and rotational DOFs is introduced, the stiffness and rotatory inertia related to rotational DOFs influence the vibration in lateral DOFs. These effects could be considered as an alternating load applied to the transverse vibration. As a result, the energy distribution of crack rotor system becomes complex. With the cracked rotor speeding up, coupling effect becomes significant and sufficient to excite a series of new frequency components (defined

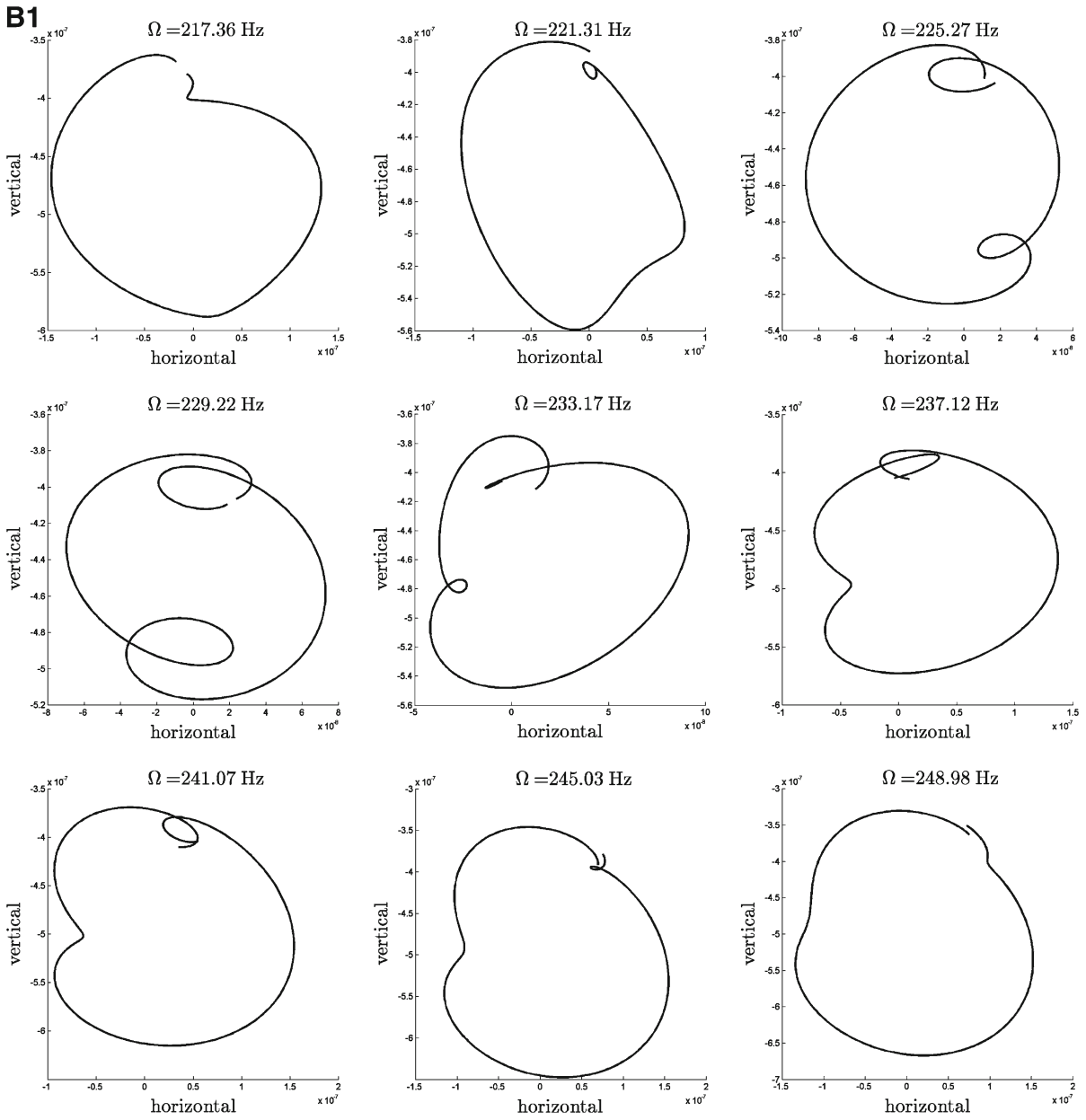

Fig. 14 continued

as perturbation frequency components). And these perturbation frequency components are separated from the unbalance response, which is represented by the harmonic components in frequency spectra. For stubby rotor, the rotatory inertia and shear effects are prominent. So the perturbation frequency components could be observed in a lower rotating speed. However, with the further increase in rotating speed, the centrifugal force grows rapidly. If the speed becomes high enough, then the alternating load introduced by coupling effect is insignificant by contrast. So the perturbation components tend to move to the harmonic components and finally joint back to the harmonic components again.

Monitoring orbit response of rotor is also a way of detecting the existence of crack in the rotor system as explained by Sinou and Lees [35]. By applying SDCM,

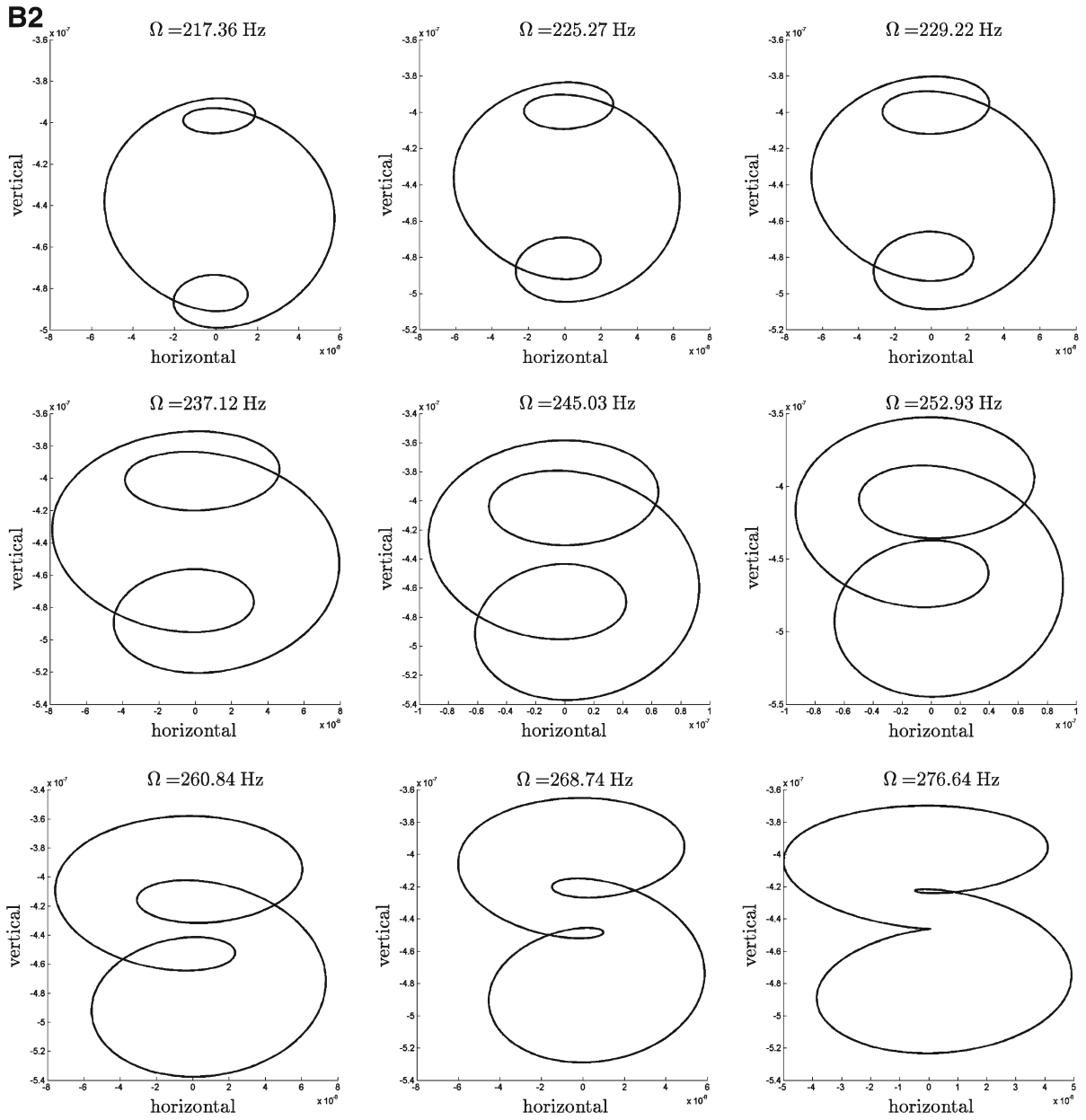

Fig. 14 continued

the orbit shapes of the given cracked rotor during passage through the sub-critical rotating speeds are illustrated in Fig. 14a1, b1. The orbit shape changes from one loop to a double loop when the rotating speed of the cracked rotor is passing through half of critical speed. An inner loop appears and becomes larger gradually; then, it turns to smaller until disappears from the outer loop. The small distortion in the orbit changes its orientation by $\frac{\pi}{2}$ during this process. When the rotating speed passes through the 1/3 of the critical speed, the orbit with two inner loops experiences a similar history. These features in the orbit response are considered as a strong evidence of the breathing crack [2,5,36]. To discover effects of three rotational DOFs on the orbit response, the whirling orbits are plotted again with the three rotational DOFs omitted as shown in Fig. 14a2,

b2. In this case, the orbit changes following a similar rule, from the whole view. However, it can be find that with the increment in rotating speed, the whirling orbit changes slower than that of SDCM. So the speed step length must be increased to observe the whole changing process.

5 Conclusion

The previous method to calculate the crack additional flexibility for rotor is modified to include more coupling mechanisms. The six DOFs coupled equations of motion of a cracked Jeffcott rotor are formulated. The effect of breathing behavior of the cracked rotor is studied with various parameters. The dynamic response of the cracked rotor is simulated with non-linear breathing crack SDCM accounting the partial crack opening. Based on the numerical investigations, the following conclusions could be extracted.

By considering the contribution of general transverse forces to the mode I crack, some coupling mechanisms are introduced. The crack additional flexibility elements obtained are consistent with the experiment result for a wide range of depth ratio. And their variation with the position of CCL coincides with literature.

When coupling mechanism between translational DOFs and rotational DOFs is introduced, a perturbation frequency component and its combination with harmonic frequencies could be observed in the response. The influence of the system parameters on the perturbation frequency is discovered. The physical explanations for these newly found frequency components are discussed in detail. The whirling orbit obtained by TDCM is a bit different from that obtained by SDCM. The evolution of the former is slower, when rotating speed is passing through the sub-critical speeds. The present study is expected to be helpful to on-line monitoring and health detecting of rotating machine.

Acknowledgments This work is grateful to the National Basic Research Program of China (Grant No. 2013CB035704).

Appendix 1: SIFs due to the six general forces

SIFs for mode I crack duo to general forces $Q_3,\ Q_4,\ Q_5$, and Q_6 :

$$K_3^{\mathrm{I}} = \sigma_3^{\mathrm{I}}\sqrt{\pi\alpha}F_2(\alpha/\alpha'),\quad \sigma_2^{\mathrm{I}} = Q_3\Big/\left(\pi R^2\right), \tag{18}$$

$$K_4^{\mathrm{I}} = \sigma_4^{\mathrm{I}}\sqrt{\pi\alpha}F_2(\alpha/\alpha'),\quad \sigma_4^{\mathrm{I}}(w) = Q_4 w\Big/\left(\frac{\pi R^4}{4}\right), \tag{19}$$

$$K_5^{\mathrm{I}} = \sigma_5^{\mathrm{I}}\sqrt{\pi\alpha}F_1(\alpha/\alpha'),\quad \sigma_5^{\mathrm{I}}(w) = Q_5\frac{\alpha'}{2}\Big/\left(\frac{\pi R^4}{4}\right), \tag{20}$$

$$K_6^{\mathrm{I}} = 0. \tag{21}$$

SIFs for mode II crack duo to six general forces:

$$K_1^{\mathrm{II}} = \tau_1^{\mathrm{II}}\sqrt{\pi\alpha}F_{\mathrm{II}}(\alpha/\alpha'),\quad \tau_1^{\mathrm{II}} = \kappa Q_1\Big/\left(\pi R^2\right), \tag{22}$$

$$K_2^{\mathrm{II}} = K_3^{\mathrm{II}} = K_4^{\mathrm{II}} = K_5^{\mathrm{II}} = 0, \tag{23}$$

$$K_6^{\mathrm{II}} = \tau_6^{\mathrm{II}}\sqrt{\pi\alpha}F_{\mathrm{III}}(\alpha/\alpha'),\ \tau_6^{\mathrm{II}}(w) = Q_6 w\Big/\left(\frac{\pi R^4}{2}\right). \tag{24}$$

SIFs for mode III crack duo to six general forces:

$$K_1^{\mathrm{III}} = K_3^{\mathrm{III}} = K_4^{\mathrm{III}} = K_5^{\mathrm{III}} = 0, \tag{25}$$

$$K_2^{\mathrm{III}} = \tau_2^{\mathrm{III}}\sqrt{\pi\alpha}F_{\mathrm{III}}(\alpha/\alpha'),\quad \tau_2^{\mathrm{III}} = \kappa Q_2/\left(\pi R^2\right), \tag{26}$$

$$K_6^{\mathrm{III}} = \tau_6^{\mathrm{III}}\sqrt{\pi\alpha}F_{\mathrm{III}}(\alpha/\alpha'),\quad \tau_6^{\mathrm{III}}(w) = Q_6\frac{\alpha'}{2}\Big/\left(\frac{\pi R^4}{2}\right), \tag{27}$$

where K_n^M is the contribution of general force Q_n ($n = 1, 2, \ldots, 6$) to the SIFs for $M = \mathrm{I},\ \mathrm{II},\ \mathrm{III}$ modes crack, and $\kappa = 6(1+\nu)/(7+6\nu)$ is shear shape coefficient of the circular beam section, ans ν is the Poisson ratio. $F_1,\ F_2,\ F_{\mathrm{II}},\ F_{\mathrm{III}}$ are dimensionless correction factors:

$$\begin{aligned}
F_1(\alpha/\alpha') &= \sqrt{\frac{2\alpha'}{\pi\alpha}\tan\left(\frac{\pi\alpha}{2\alpha'}\right)}\\
&\times\frac{0.923+0.199[1-\sin(\pi\alpha/2\alpha')]^4}{\cos(\pi\alpha/2\alpha')},\\
F_2(\alpha/\alpha') &= \sqrt{\frac{2\alpha'}{\pi\alpha}\tan\left(\frac{\pi\alpha}{2\alpha'}\right)}\\
&\times\frac{0.752+2.02(\alpha/\alpha')+0.37[1-\sin(\pi\alpha/2\alpha')]^3}{\cos(\pi\alpha/2\alpha')},\\
F_{\mathrm{II}}(\alpha/\alpha') &= \Big[1.122-0.561(\alpha/\alpha')+0.085(\alpha/\alpha')^2\\
&+0.18(\alpha/\alpha')^3\Big]/\sqrt{1-\alpha/\alpha'},\\
F_{\mathrm{III}}(\alpha/\alpha') &= \sqrt{\frac{2\alpha'}{\pi\alpha}\tan\left(\frac{\pi\alpha}{2\alpha'}\right)}.
\end{aligned} \tag{28}$$

Appendix 2: elements of crack additional flexibility matrix

The non-zero elements of the crack additional flexibility 6×6 matrix are as shown below:

$$g_{11}^{\text{crack}} = \frac{2(1-\upsilon^2)}{\pi E R^8} \times \int \alpha \left[F_{\text{I}}^2 L^2 \left(R^2 - w^2 \right) + F_{\text{II}} R^4 \kappa^2 \right] \mathrm{d}A, \quad (29)$$

$$g_{12}^{\text{crack}} = g_{21}^{\text{crack}} = \frac{2(1-\upsilon^2)}{\pi E R^8} \times \int F_{\text{I}} F_2 L^2 w \alpha \sqrt{R^2 - w^2} \mathrm{d}A, \quad (30)$$

$$g_{13}^{\text{crack}} = g_{31}^{\text{crack}} = \frac{2(1-\upsilon^2)}{\pi E R^6} \times \int F_{\text{I}} F_2 L \alpha \sqrt{R^2 - w^2} \mathrm{d}A, \quad (31)$$

$$g_{14}^{\text{crack}} = g_{41}^{\text{crack}} = \frac{8(1-\upsilon^2)}{\pi E R^8} \times \int F_{\text{I}} F_2 L w \alpha \sqrt{R^2 - w^2} \mathrm{d}A, \quad (32)$$

$$g_{15}^{\text{crack}} = g_{51}^{\text{crack}} = \frac{8(1-\upsilon^2)}{\pi E R^8} \times \int F_{\text{I}}^2 L \alpha \left(R^2 - w^2 \right) \mathrm{d}A, \quad (33)$$

$$g_{16}^{\text{crack}} = g_{61}^{\text{crack}} = \frac{4(1-\upsilon^2)}{\pi E R^6} \int F_{\text{II}}^2 \kappa w \alpha \mathrm{d}A, \quad (34)$$

$$g_{22}^{\text{crack}} = \frac{2(1+\upsilon)}{\pi E R^8} \times \int \alpha \left[F_{\text{III}}^2 R^4 \kappa^2 + F_2^2 L^2 w^2 (1-\upsilon) \right] \mathrm{d}A, \quad (35)$$

$$g_{23}^{\text{crack}} = g_{32}^{\text{crack}} = \frac{2(1-\upsilon^2)}{\pi E R^6} \int F_2^2 L w \alpha \mathrm{d}A, \quad (36)$$

$$g_{24}^{\text{crack}} = g_{42}^{\text{crack}} = \frac{8(1-\upsilon^2)}{\pi E R^8} \int F_2^2 L w^2 \alpha \mathrm{d}A, \quad (37)$$

$$g_{25}^{\text{crack}} = g_{52}^{\text{crack}} = \frac{8(1-\upsilon^2)}{\pi E R^8} \times \int F_{\text{I}} F_2 L w \alpha \sqrt{R^2 - w^2} \mathrm{d}A, \quad (38)$$

$$g_{26}^{\text{crack}} = g_{62}^{\text{crack}} = \frac{4(1+\upsilon)}{\pi E R^6} \times \int F_{\text{III}}^2 \kappa \alpha \sqrt{R^2 - w^2} \mathrm{d}A, \quad (39)$$

$$g_{33}^{\text{crack}} = \frac{2(1-\upsilon^2)}{\pi E R^4} \int F_2^2 \alpha \mathrm{d}A, \quad (40)$$

$$g_{34}^{\text{crack}} = g_{43}^{\text{crack}} = \frac{8(1-\upsilon^2)}{\pi E R^6} \int F_2^2 w \alpha \mathrm{d}A, \quad (41)$$

$$g_{35}^{\text{crack}} = g_{53}^{\text{crack}} = \frac{8(1-\upsilon^2)}{\pi E R^6} \times \int F_{\text{I}} F_2 \alpha \sqrt{R^2 - w^2} \mathrm{d}A, \quad (42)$$

$$g_{44}^{\text{crack}} = \frac{32(1-\upsilon^2)}{\pi E R^8} \int F_2^2 w^2 \alpha \mathrm{d}A, \quad (43)$$

$$g_{45}^{\text{crack}} = g_{54}^{\text{crack}} = \frac{32(1-\upsilon^2)}{\pi E R^8} \times \int F_{\text{I}} F_2 w \alpha \sqrt{R^2 - w^2} \mathrm{d}A, \quad (44)$$

$$g_{55}^{\text{crack}} = \frac{32(1-\upsilon^2)}{\pi E R^8} \int F_{\text{I}}^2 \alpha \left(R^2 - w^2 \right) \mathrm{d}A, \quad (45)$$

$$g_{66}^{\text{crack}} = \frac{8(1+\upsilon)}{\pi E R^8} \times \int \alpha \left[F_{\text{III}}^2 R^2 + F_{\text{II}}^2 w^2 - F_{\text{III}}^2 w^2 (1-\upsilon) \right] \mathrm{d}A. \quad (46)$$

References

1. Dimarogonas, A.D., Paipetis, S.A.: Analytical Methods in Rotor Dynamics. Applied Science Publisher, London (1983)
2. Darpe, A.K., Gupta, K., Chawla, A.: Transient response and breathing behaviour of a cracked Jeffcott rotor. J. Sound Vib. **272**(1–2), 207–243 (2004)
3. Jun, O.S., Eun, H.J., Earmme, Y.Y., Lee, C.W.: Modeling and vibration analysis of a simple rotor with a breathing crack. J. Sound Vib. **155**(2), 273–290 (1992)
4. Papadopoulos, C.A., Dimarogonas, A.D.: Coupled longitudinal and bending vibrations of a rotating shaft with an open crack. J. Sound Vib. **117**(1), 81–93 (1987)
5. Patel, T.H., Darpe, A.K.: Influence of crack breathing model on nonlinear dynamics of a cracked rotor. J. Sound Vib. **311**(3–5), 953–972 (2008)
6. Rubio, L., Fernandez-Saez, J.: A new efficient procedure to solve the nonlinear dynamics of a cracked rotor. Nonlinear Dyn. **70**(3), 1731–1745 (2012)
7. Papadopoulos, C.A.: The strain energy release approach for modeling cracks in rotors: a state of the art review. Mech. Syst. Signal Process. **22**(4), 763–789 (2008)
8. Al-Shudeifat, M.A.: On the finite element modeling of the asymmetric cracked rotor. J. Sound Vib. **332**(11), 2795–2807 (2013)
9. Al-Shudeifat, M.A., Butcher, E.A.: New breathing functions for the transverse breathing crack of the cracked rotor system: approach for critical and subcritical harmonic analysis. J. Sound Vib. **330**(3), 526–544 (2011)
10. Guo, C., Al-Shudeifat, M.A., Yan, J., Bergman, L.A., McFarland, D.M., Butcher, E.A.: Application of empirical mode decomposition to a Jeffcott rotor with a breathing crack. J. Sound Vib. **332**(16), 3881–3892 (2013)

11. Guo, C.Z., Al-Shudeifat, M.A., Yan, J.H., Bergman, L.A., McFarland, D.M., Butcher, E.A.: Stability analysis for transverse breathing cracks in rotor systems. Eur. J. Mech. A **42**, 27–34 (2013)
12. Kulesza, Z., Sawicki, J.T.: Rigid finite element model of a cracked rotor. J. Sound Vib. **331**(18), 4145–4169 (2012)
13. Kulesza, Z., Sawicki, J.T.: New finite element modeling approach of a propagating shaft crack. J. Appl. Mech. Trans. ASME **80**(2), 021025 (2013)
14. Ostachowicz, W., Krawczuk, M.: Coupled torsional and bending vibrations of a rotor with an open crack. Arch. Appl. Mech. **62**(3), 191–201 (1992)
15. Qin, W.Y., Chen, G.R., Ren, X.M.: Grazing bifurcation in the response of cracked Jeffcott rotor. Nonlinear Dyn. **35**(2), 147–157 (2004)
16. Ballo, I.: Non-linear effects of vibration of a continuous transverse cracked slender shaft. J. Sound Vib. **217**(2), 321–333 (1998)
17. Wauer, J.: Modelling and formulation of equations of motion for cracked rotating shafts. Int. J. Solids Struct. **26**(8), 901–914 (1990)
18. Lee, C.W., Yun, J.S., Jun, O.S.: Modeling of a simple rotor with a switching crack and its experimental-verification. J. Vib. Acoust. **114**(2), 217–225 (1992)
19. Chondros, T.G., Dimarogonas, A.D., Yao, J.: Vibration of a beam with a breathing crack. J. Sound Vib. **239**(1), 57–67 (2001)
20. Mayes, I.W., Davies, W.G.R.: Analysis of the response of a multi-rotor-bearing system containing a transverse crack in a rotor. J. Vib. Acoust. Stress **106**(1), 139–145 (1984)
21. Chen, C., Dai, L.: Bifurcation and chaotic response of a cracked rotor system with viscoelastic supports. Nonlinear Dyn. **50**(3), 483–509 (2007)
22. Darpe, A.K., Chawla, A., Gupta, K.: Analysis of the response of a cracked Jeffcott rotor to axial excitation. J. Sound Vib. **249**(3), 429–445 (2002)
23. Darpe, A.K., Gupta, K., Chawla, A.: Experimental investigations of the response of a cracked rotor to periodic axial excitation. J. Sound Vib. **260**(2), 265–286 (2003)
24. Papaeconomou, N., Dimarogonas, A.: Vibration of cracked beams. Comput. Mech. **5**(2–3), 88–94 (1989)
25. Chen, C.P., Dai, L.M., Fu, Y.M.: Nonlinear response and dynamic stability of a cracked rotor. Commun. Nonlinear Sci. **12**(6), 1023–1037 (2007)
26. Fu, Y.M., Zheng, Y.F., Hou, Z.K.: Analysis of non-linear dynamic stability for a rotating shaft-disk with a transverse crack. J. Sound Vib. **257**(4), 713–731 (2002)
27. Han, Q.K., Chu, F.L.: The effect of transverse crack upon parametric instability of a rotor-bearing system with an asymmetric disk. Commun. Nonlinear Sci. **17**(12), 5189–5200 (2012)
28. Han, Q.K., Chu, F.L.: Parametric instability of a Jeffcott rotor with rotationally asymmetric inertia and transverse crack. Nonlinear Dyn. **73**(1–2), 827–842 (2013)
29. Meng, G., Gasch, R.: Stability and stability degree of a cracked flexible rotor supported on journal bearings. J. Vib. Acoust. **122**(2), 116–125 (2000)
30. Sekhar, A.S., Dey, J.K.: Effects of cracks on rotor system instability. Mech. Mach. Theory **35**(12), 1657–1674 (2000)
31. Sinou, J.J.: Effects of a crack on the stability of a non-linear rotor system. Int. J. Nonlinear Mech. **42**(7), 959–972 (2007)
32. Bush, A.J.: Experimentally determined stress-intensity factors for single-edge crack round bars loaded in bending. Exp. Mech. **16**(7), 249–257 (1976)
33. Darpe, A.K., Gupta, K., Chawla, A.: Coupled bending, longitudinal and torsional vibrations of a cracked rotor. J. Sound Vib. **269**(1–2), 33–60 (2004)
34. Tada, H., Paris, P.C., Irwin, G.R.: The Stress Analysis of Cracks Handbook, 3rd edn. ASME Press, New York (2000)
35. Sinou, J.J., Lees, A.W.: The influence of cracks in rotating shafts. J. Sound Vib. **285**(4–5), 1015–1037 (2005)
36. Al-Shudeifat, M.A., Butcher, E.A., Stern, C.R.: General harmonic balance solution of a cracked rotor-bearing-disk system for harmonic and sub-harmonic analysis: analytical and experimental approach. Int. J. Eng. Sci. **48**(10), 921–935 (2010)